





**Emission ghost imaging: Reconstruction with data augmentation**K. J. Coakley <sup>\*</sup>*National Institute of Standards and Technology, 325 Broadway, Boulder, Colorado 80305, USA*H. H. Chen-Mayer , B. Ravel , D. Josell , N. N. Klimov, and D. S. Hussey *National Institute of Standards and Technology, 100 Bureau Drive, Gaithersburg, Maryland 20899, USA*S. M. Robinson <sup>†</sup>*Physical Measurement Laboratory, National Institute of Standards and Technology, Gaithersburg, Maryland 20899, USA  
and Department of Materials Science and Engineering, University of Maryland, College Park, Maryland 20742-2115, USA*

(Received 30 September 2023; revised 8 December 2023; accepted 2 January 2024; published 1 February 2024)

Ghost imaging enables two-dimensional reconstruction of an object even though particles transmitted or emitted by the object of interest are detected with a single pixel detector without spatial resolution. This is possible because for the particular implementation of ghost imaging presented here, the incident beam is spatially modulated with a nonconfigurable attenuating mask whose orientation is varied (e.g. via transverse displacement or rotation) in the course of the ghost imaging experiment. Each orientation yields a distinct spatial pattern in the attenuated beam. In many cases ghost imaging reconstructions can be dramatically improved by factoring the measurement matrix which consists of measured attenuated incident radiation for each of many orientations of the mask at each pixel to be reconstructed as the product of an orthonormal matrix  $Q$  and an upper triangular matrix  $R$ , provided that the number of orientations of the mask ( $N$ ) is greater than or equal to the number of pixels ( $P$ ) reconstructed. For the  $N < P$  case, we present a data augmentation method that enables  $QR$  factorization of the measurement matrix. To suppress noise in the reconstruction, we determine the Moore-Penrose pseudoinverse of the measurement matrix with a truncated singular value decomposition approach. Since the resulting reconstruction is still noisy, we denoise it with the adaptive weights smoothing method. In simulation experiments our method outperforms a modification of an existing alternative orthogonalization method where rows of the measurement matrix are orthogonalized by the Gram-Schmidt method. We apply our ghost imaging methods to experimental x-ray fluorescence data acquired at Brookhaven National Laboratory.

DOI: [10.1103/PhysRevA.109.023501](https://doi.org/10.1103/PhysRevA.109.023501)**I. INTRODUCTION**

Although first applied to quantum optics [1,2], ghost imaging also has classical applications, including experiments with pseudorandom light [3], x rays [4–7], electrons [8] and neutrons [9] (all of which are in transmission mode) and lidar [10] (in reflection mode). Recently, an implementation of ghost imaging, in emission mode, was developed for elemental mapping based on x-ray fluorescence signals [11,12]. Here we focus on ghost imaging of spatially varying emission yields. Ghost imaging is attractive because it may enable high-quality reconstructions with lower doses of incident radiation than doses associated with traditional methods [13]. Further, detected particles need not be collimated in ghost imaging. This aspect of ghost imaging is important because in some applications (e.g., possible emission ghost imaging based on prompt  $\gamma$  rays produced by neutron illumination [9]), collimation is not feasible.

In ghost imaging with penetrating radiation such as neutrons or x rays, the incident beam is attenuated by a nonconfigurable mask whose orientation is varied (e.g., via transverse displacement or rotation) in the course of the ghost imaging experiment. At each mask orientation, the spatial variation of the attenuated incident beam is distinct. Without the object of interest, one acquires measurements of the attenuated incident beam at each pixel due to each mask orientation with a position sensitive detector. This data forms the measurement matrix  $A$ . With only the object of interest placed behind the mask, for each mask orientation the total number of particles transmitted through the object (or particles emitted by the object) is (ideally) detected by a single pixel detector termed the bucket detector. In practice, the total solid angle subtended by the bucket detector about any location in the object where emission occurs is less than  $4\pi$ . Hence, the expected fractions of emitted particles that are detected in emission ghost imaging experiments depend on solid angle effects and detector efficiency. Reconstructions are determined given the “bucket” data and the measurement matrix.

In many applications, ghost imaging reconstructions can be dramatically improved when the measurement matrix  $A$  is factored as the product of an orthonormal matrix  $Q$  and an

<sup>\*</sup>kevin.coakley@nist.gov<sup>†</sup>Current address: Sensor Science Division, Physical Measurement Laboratory, National Institute of Standards and Technology, Gaithersburg, Maryland 20899, USA.

upper triangular matrix  $R$  (see, for example, [6]). However,  $QR$  factorization of  $A$  is not feasible when the number of mask orientations  $N$  is less than the number of pixels  $P$  that are reconstructed. As discussed in [14], the  $N < P$  case is not rare. For the  $N < P$  case, we present a data augmentation method that increases  $N$  and enables  $QR$  factorization of the augmented measurement matrix. We remark that noisy training data is often extended in machine learning studies with data augmentation methods (see, for example, [15,16]). However, these methods are very different from our data augmentation method.

Our reconstruction algorithm based on the  $QR$  factorization of the measurement matrix is similar to the method in [6]. However, unlike in [6], we suppress noise effects by determining the Moore-Penrose pseudoinverse [17–19] of the measurement matrix with a truncated singular value decomposition (TSVD) method [20,21]. We note that Chen *et al.* [22] implemented a TSVD method for ghost imaging with a reconstruction method that differs from our  $QR$  method. In general, reconstructions obtained with our method are still noisy, hence we denoise them with the adaptive weight smoothing (AWS) method [23–25]. Like wavelet methods, AWS can smooth out noise while preserving edges in images. For other denoising methods for ghost imaging, see, for example, Refs. [26–28].

In Sec. II we discuss our ghost imaging reconstruction method, our data augmentation method, and the adaptive weights smoothing method. In Sec. III A, in a simulation study we demonstrate that our method yields reconstructions with lower root-mean-square error (RMSE) than reconstructions obtained by a modified version of an existing method [14] where the rows of the measurement matrix are orthogonalized with a Gram-Schmidt procedure rather than a  $QR$  method. In Sec. III B we apply our ghost imaging methods to experimental x-ray fluorescence data acquired at Brookhaven National Laboratory. In Sec. IV we discuss results and summarize some diagnostic studies.

## II. METHODS

### A. Reconstruction method: No $QR$ step

First we define the measurement matrix  $A$ . Since the photon imaging detector acquires a two-dimensional (2D) image of size  $6 \times 46$ , there are 276 pixels. We assign an index to each pixel. For instance, the pixel indexes in the first row of the photon image detector range from 1 to 46. In the second row they range from 47 to 92. And so on. The  $ij$ (th) element of  $A$  corresponds to the measured attenuated incident beam produced by the  $i$ th mask orientation at the  $j$ th pixel. The size of  $A$  is  $N \times P$ , where  $N$  is the number of mask orientations and  $P$  is the number of pixels. For instance, if we reconstruct an image of size  $6 \times 46$ ,  $P = 276$ . We define the theoretical measurement matrix to be  $\tilde{A}$ . By theoretical we mean what would be observed in an ideal experiment without measurement errors. We define the observed and theoretical bucket data vectors to be  $b$  and  $\tilde{b}$ , respectively. Both  $b$  and  $\tilde{b}$  are  $N$ -dimensional vectors. The  $i$ th component of  $b$ ,  $b_i$  is the observed number of events detected by the bucket detector for the  $i$ th orientation of the attenuating mask. Given the theoretical measurement

matrix  $\tilde{A}$  and theoretical emission yield vector  $\tilde{v}$ , we have that

$$\tilde{A}\tilde{v} = \tilde{b}. \quad (1)$$

This theoretical relationship applies to transmission ghost imaging as well. For experimental data, due to measurement error we have that

$$Av \approx b. \quad (2)$$

Based on  $A$  and  $b$ , our estimate of  $\tilde{v}$  is  $v$ . Below we describe our approach to estimate  $\tilde{v}$ .

The ghost imaging estimate of  $\tilde{v}$  (which can be an attenuation term for transmission studies or an emission term like in our study) at the pixel centered at  $(x, y)$ ,  $v(x, y)$ , satisfies the following equation (see Eq. (7) of [6]):

$$v(x, y) * PSF(x, y) = \frac{1}{N} \sum_{i=1}^N (b_i - \bar{b}) I_i(x, y), \quad (3)$$

where  $*$  denotes convolution,  $N$  is the number of mask orientations,  $I_i(x, y)$  is the measured attenuated incident beam at location  $(x, y)$  due to the  $i$ th orientation of the attenuating mask, and  $\bar{b} = \frac{1}{N} \sum_{i=1}^N b_i$ . In the ghost imaging literature, for masks that are spatially random, the set of  $I_i(x, y)$  is typically referred to as a speckle basis. To simplify calculations we assume that  $(x, y) = \bar{x}_j$ , where  $j$  is an integer between 1 and  $P$  and  $\bar{x}_j = (x_j, y_j)$  is the midpoint of the  $j$ th pixel. Similarly,  $\bar{x}_k = (x_k, y_k)$  is the midpoint of the  $k$ th pixel. For estimation of  $\tilde{v}$ , based on the ‘‘approximate completeness relation’’ discussed in Sec. 4.1 of [6] and Eq. (14) in [6], we model the  $PSF$  as

$$PSF(\bar{x}_j - \bar{x}_k) = \frac{1}{N} \sum_{i=1}^N [I_i(\bar{x}_k) - \bar{I}(\bar{x}_k)] \times [I_i(\bar{x}_j) - \bar{I}(\bar{x}_j)] \delta_{j,k}, \quad (4)$$

where

$$\begin{aligned} \bar{I}(\bar{x}_j) &= \frac{1}{N} \sum_{i=1}^N I_i(\bar{x}_j), \\ \bar{I}(\bar{x}_k) &= \frac{1}{N} \sum_{i=1}^N I_i(\bar{x}_k), \end{aligned} \quad (5)$$

and  $\delta_{j,k}$  is the Kronecker  $\delta$  function. We get that

$$\begin{aligned} v(\bar{x}_j) * PSF(\bar{x}_j) &= \sum_{k=1}^P v(\bar{x}_k) PSF(\bar{x}_j - \bar{x}_k) \\ &= \frac{v(\bar{x}_j)}{N} \sum_{i=1}^N [I_i(\bar{x}_j) - \bar{I}(\bar{x}_j)]^2. \end{aligned} \quad (6)$$

Rewriting with  $\bar{x}_j$  substituted with  $(x, y)$  yields

$$v(x, y) * PSF(x, y) = \frac{v(x, y)}{N} \sum_{i=1}^N [I_i(x, y) - \bar{I}(x, y)]^2, \quad (7)$$

where

$$\bar{I}(x, y) = \frac{1}{N} \sum_{i=1}^N I_i(x, y). \quad (8)$$

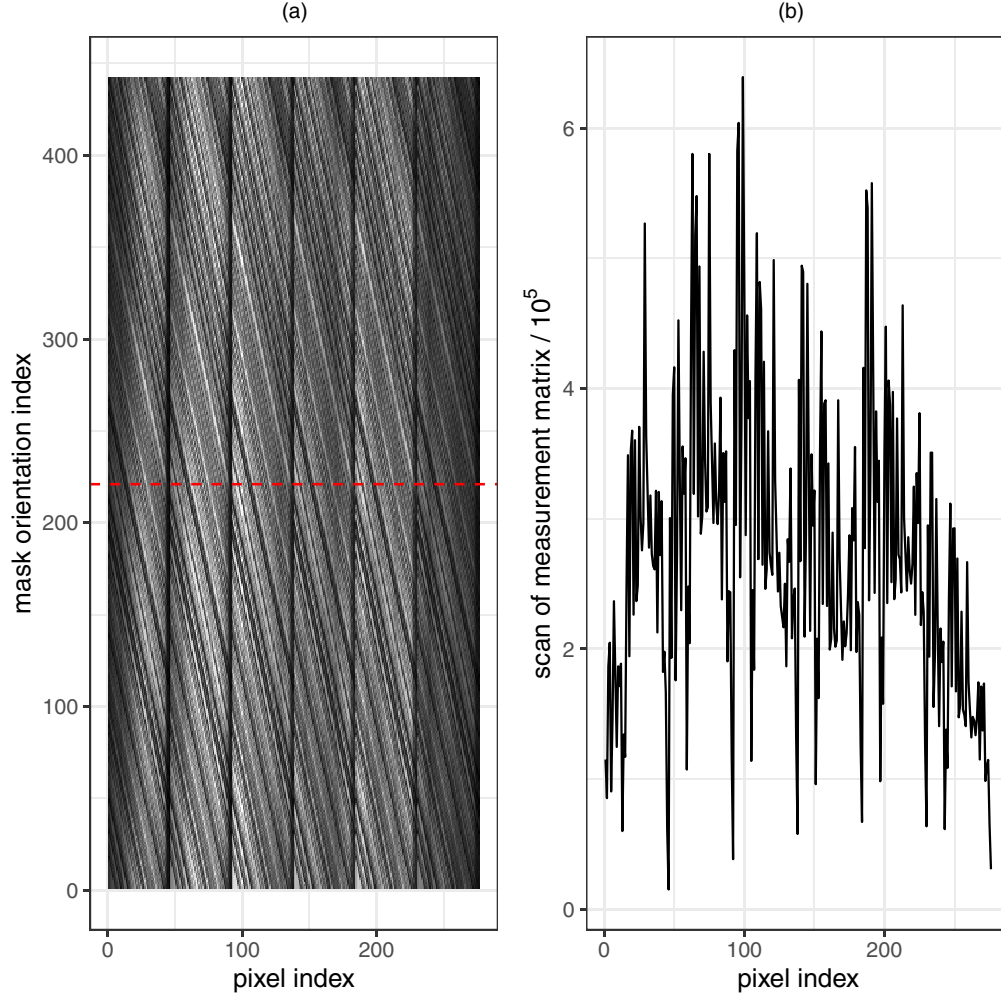


FIG. 1. (a) Experimental measurement matrix acquired at Brookhaven National Laboratory. (b) Scan of measurement matrix [corresponding to red dashed line in (a)].

Further simplifying, we get that

$$v(x, y) = \frac{1}{N-1} \sum_{i=1}^N (b_i - \bar{b}) \frac{I_i(x, y)}{\hat{\sigma}_{I(x,y)}^2}, \quad (9)$$

where  $\hat{\sigma}_{I(x,y)}^2$  is the sample variance of  $I_1(x, y), I_2(x, y), \dots, I_N(x, y)$ . For a definition of the sample variance, see, for example, Ref. [29]. We note that our Eq. (9) result has some similarity with a result based on random matrix theory (see Eq. (14) of [7]).

In our simulation studies each photon is detected with probability 1. For cases where each photon is detected with probability  $p_{\text{det}} < 1$ , one would scale  $v(x, y)$  by  $1/p_{\text{det}}$ . A similar comment may apply to emission ghost imaging of experimental data.

Based on Eq. (9), we can express  $v$  as

$$v = \frac{1}{N-1} W A^T (b - \bar{b} \bar{\mathbf{1}}), \quad (10)$$

where  $\bar{\mathbf{1}}$  is an  $N$ -dimensional vector where each component is 1,  $A^T$  is the transpose of  $A$ , and  $W$  is a diagonal matrix of size

$P \times P$ , where the  $k$ th diagonal value of  $W$  is  $1/\hat{\sigma}^2(k)$ . We note that in many ghost imaging papers,  $W$  is neglected. After we obtain the  $P$ -dimensional  $v$ , we form the 2D reconstruction of interest by mapping the components of the vector  $v$  into a matrix.

### B. Reconstruction with $QR$ method

Following Appendix B of [6], for the case  $N > P$  we factor the measurement matrix  $A$  as

$$A = QR, \quad (11)$$

where  $Q$  is an orthonormal matrix of size  $N \times P$ , and  $R$  is an upper triangular matrix of size  $P \times P$ . We replace  $A$  with  $Q$ , and  $b$  with  $QA^+b$ , where  $A^+$  is the Moore-Penrose pseudoinverse of  $A$ . To suppress noise effects, we determine  $A^+$  based on the TSVD of  $A$ . In this approach terms in the singular value decomposition (SVD) with singular values below the product of the maximum singular value and an adjustable relative threshold  $\kappa_{\text{SVD}}$  are excluded. For detailed discussions on computation of the truncated SVD of  $A$  and  $A^+$  (based on the truncated SVD of  $A$ ), see Refs. [20,21]. We obtain the recon-

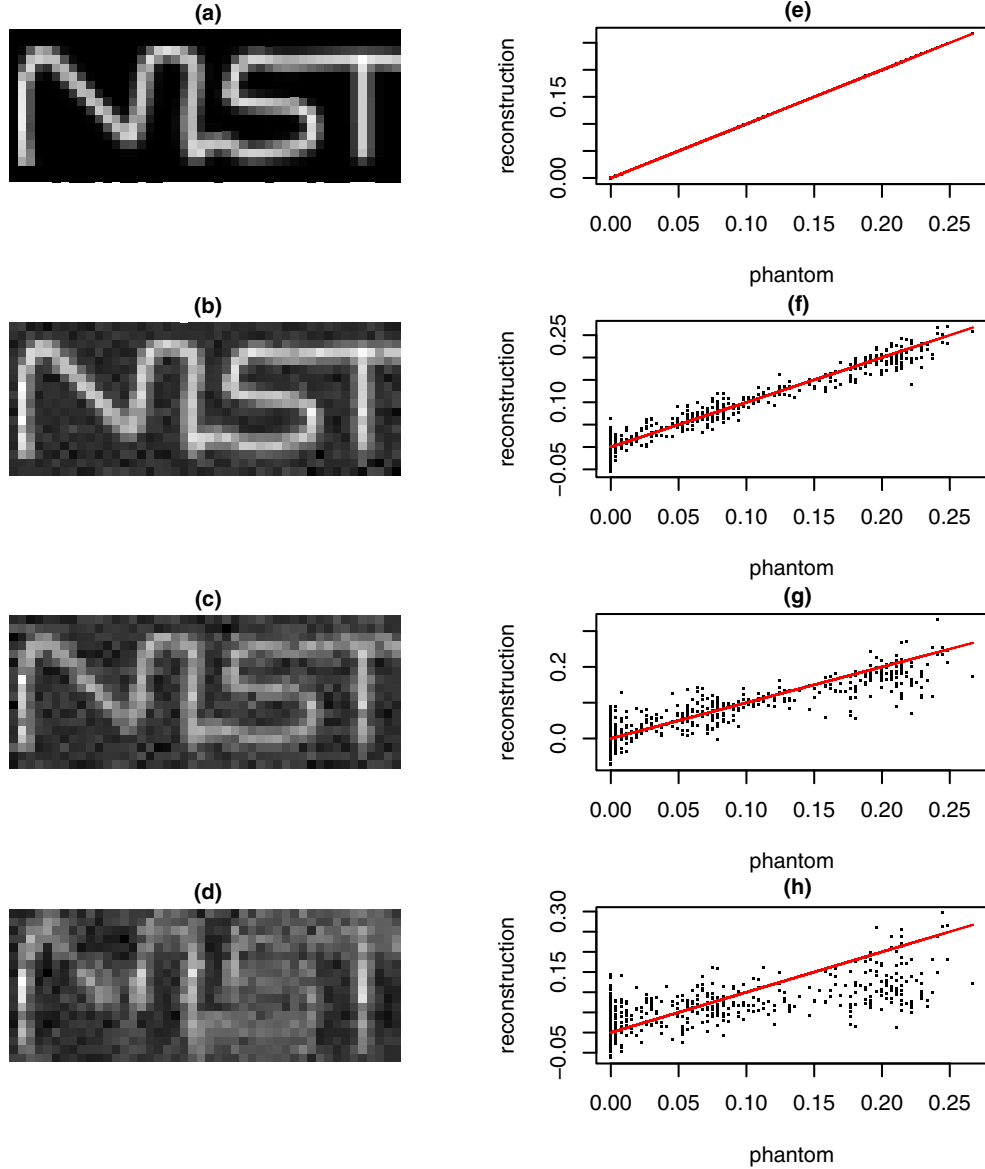


FIG. 2. The number of pixels is  $P = 276$ . We equate the theoretical measurement matrix to 10 times the experimental measurement matrix shown in Fig. 1. Here we show reconstructions of noise-free data determined with data augmentation,  $QR$  and TSVD steps where the relative threshold for the truncated SVD method,  $\kappa_{\text{SVD}}$ , is  $1.49 \times 10^{-8}$ . (a)–(d) Reconstructions for  $N = 275, 250, 200,$  and  $100$ . (e)–(h) Associated scatterplots of reconstructions and the digital phantom. Points that fall on the red line correspond to cases where the reconstruction and true value agree exactly.

struction of  $\tilde{v}$  with Eq. (9) [or equivalently, Eq. (10)]. Similar to methods in [6], we obtain a reconstruction for each of many permutations of the columns of  $A$  (before the  $QR$  step). For each pixel the final reconstruction is the median value of all the reconstructions. Since the reconstruction depends on the order of the columns, the permutation method can suppress noise effects. To get a permutation of the columns of  $A$ , we simulate a permutation of the integers  $(1, 2, 3, \dots, P)$ . (As in illustration, for the simple case where  $P = 4$  and the simulated values of the permuted integers are  $(3, 1, 4, 2)$ , the first, second, third, and fourth columns of the new matrix  $A$  would be the third column of the original  $A$  matrix, the first column of the original  $A$  matrix, the fourth column of the original  $A$  matrix, and the second column of the original  $A$

matrix, respectively. Because the columns are permuted, the components of  $v$  are too. That is, the first, second, third, and fourth components of  $v$  correspond to estimates for pixels 3, 1, 4, 2. Hence the components are reordered so that the order of the reconstructed values correspond to the first, second, third, and fourth pixel.) For simulated and experimental data, the number of permutations are 51 and 101, respectively. In our simulation study, for each value of  $N$  we determine the RMSE of each reconstruction on a grid in  $\kappa_{\text{SVD}}$  space by Monte Carlo simulation. For each  $N$  we select the value of  $\kappa_{\text{SVD}}$  that yields the lowest RMSE. For experimental data we determine reconstructions at various values of  $\kappa_{\text{SVD}}$  and select the best reconstruction by scientific judgment. For example, for reconstructions of experimental data, we vary  $\kappa_{\text{SVD}}$  over a

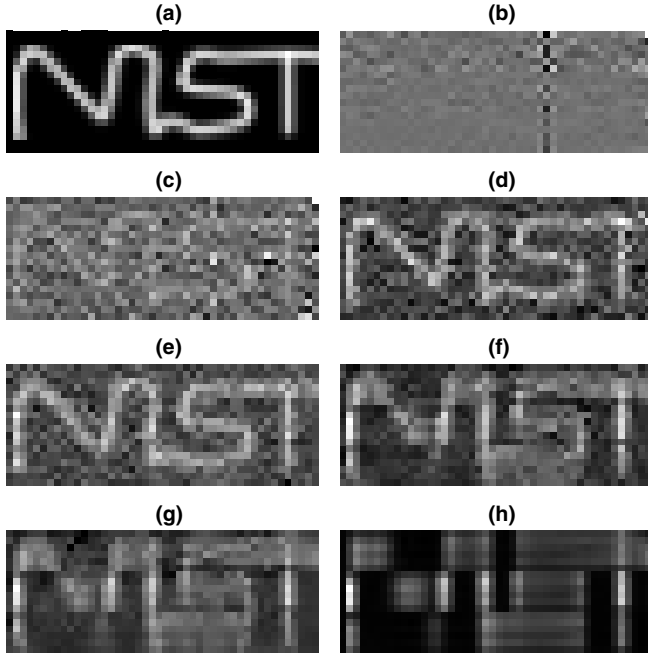


FIG. 3. We equate the theoretical measurement matrix to 10 times the experimental measurement matrix shown in Fig. 1. The number of pixels is  $P = 276$ . We show reconstructions of simulated noisy data where  $N = 275$  where  $\kappa_{\text{SVD}}$  varies. (a) Digital phantom. (b)–(i) Reconstructions where  $\kappa_{\text{SVD}} = 10^{-6}$ ,  $10^{-5}$ ,  $5 \times 10^{-5}$ ,  $10^{-4}$ ,  $5 \times 10^{-4}$ ,  $10^{-3}$ , and  $5 \times 10^{-3}$ , respectively.

grid and select the value of  $\kappa_{\text{SVD}}$  that appears to produce the reconstruction that best resembles the physical phantom. As a caveat, as discussed in Sec. IV, in future research we plan to develop data-driven methods to select  $\kappa_{\text{SVD}}$ .

### C. Data augmentation

For the  $N < P$  case, we augment  $A$  and the bucket signal  $b$ . In our simulation studies  $P = 276$  and  $N$  varies from 50 to 275. For each column of  $A$ ,  $c = (c_1, c_2, \dots, c_N)^T$ , we stack  $k$  copies of  $c$  to form an augmented column  $c_{\text{aug}}$ . The stacking parameter  $k$  is increased until  $kN \geq P$ . For instance, if  $k = 2$  the augmented column is  $c_{\text{aug}} = (c_1, c_2, \dots, c_N, c_1, c_2, \dots, c_N)^T$ . For the case  $k = 3$  the augmented column  $c_{\text{aug}} = (c_1, c_2, \dots, c_N, c_1, c_2, \dots, c_N, c_1, c_2, \dots, c_N)^T$ . Extensions for larger  $k$  are similar to the above. In our augmented measurement matrix, each column has a periodic structure. The bucket signal is augmented in a similar manner and also has a periodic structure. The dimension of the augmented bucket data vector is the same as the number of rows in the augmented measurement matrix.

### D. Reconstruction with row-orthogonalization method

For the  $N < P$  case, Luo *et al.* [14] orthogonalized the rows of the measurement matrix with a Gram-Schmidt method. Given the projection coefficients determined in the Gram-Schmidt method, the bucket signal was also transformed (see [14] for more details). Based on the transformed versions of  $A$

and  $b$ , the reconstruction is

$$v = \frac{\alpha}{N} A^T (b - \bar{b} \bar{1}), \quad (12)$$

where  $\alpha$  is an adjustable scale parameter. Initially, we determine  $v$  with Eq. (12) with  $\alpha = 1$ . Based on the predicted bucket signal,  $\hat{b} = Av$ , and the observed bucket signal  $b$ , we estimate the scaling factor  $\alpha$  as  $\hat{\alpha}$  where

$$\hat{\alpha} = \frac{b_1 + b_2 \dots + b_N}{\hat{b}_1 + \hat{b}_2 \dots + \hat{b}_N}. \quad (13)$$

We then adjust  $v$  by scaling it by  $\hat{\alpha}$ . We stress that this method for determination of  $\alpha$  is not discussed in [14]. In our primary simulation study, for the cases studied  $\hat{\alpha}$  ranges from approximately 60 to 300.

### E. Denoising with adaptive weights smoothing

We denoise reconstructions with the AWS method [23–25]. In this approach local polynomial models are fit to 2D reconstructions by maximizing a weighted log-likelihood function in the neighborhood about each spatial location. At each spatial location the denoised value is the value predicted by the local polynomial model. In the AWS method the weighted log-likelihood function at point  $x$  is modeled as

$$L(W(x), \theta) = \sum_i w_i(x) \ln p(Y_i, \theta), \quad (14)$$

where  $Y_i$  is measured at  $x_i$ ,  $w_i$  is the weight corresponding to the measured value at  $x_i$ , and the point of interest at  $x$ ,  $p$  is the likelihood of  $Y_i$  given the polynomial model parameter vector  $\theta$ . The basic idea of the AWS approach is to adaptively select the size of the neighborhood about any point of interest and the associated weights in that neighborhood. The overall smoothness of the resulting image depends on the choice of a bandwidth parameter  $h_{\text{max}}$ , which specifies the maximum size of any local neighborhood, and a parameter  $\lambda$ , which determines when to stop expanding the size of the local neighborhood about any point according to a hypothesis test criterion. In general, as  $\lambda$  increases the resulting image becomes smoother. Like wavelet methods, the AWS method can preserve edges while smoothing within regions between jumps. In our studies we equate  $h_{\text{max}}$  to 2.5 pixel lengths,  $\lambda = 1$ , and the degree of the local polynomial is 2. We implement AWS in the statistical computing language and environment R [30] by calling the function `lpaws` in the R package `aws`.

## III. RESULTS

### A. Simulation study

Our simulation model is based on experimental data acquired at Brookhaven National Laboratory (BNL). In the experiment, synchrotron x rays produce fluorescent x rays from a physical phantom. Since the incident beam flux was too narrow in the vertical direction (1 mm) to illuminate the entire physical phantom (which is 2.5 mm tall in the vertical direction), the physical phantom was translated vertically three times to ensure that the bucket data for all three regions of the physical phantom had sufficiently high signal



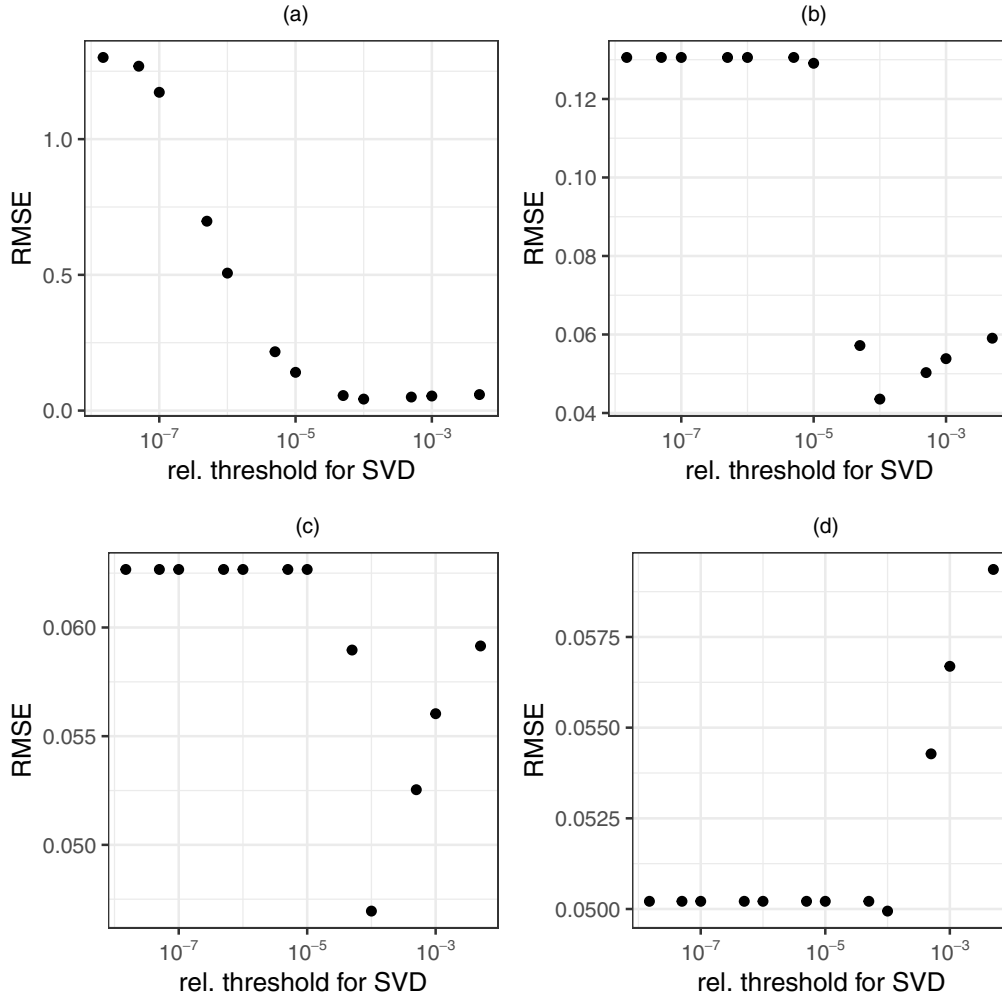


FIG. 4. We equate the theoretical measurement matrix to 10 times the experimental measurement matrix shown in Fig. 1. The number of pixels is  $P = 276$ . For our data augmentation method (with  $QR$  and TSVD steps), we show RMSE of reconstructions of simulated noisy data as a function of  $\kappa_{\text{SVD}}$ . (a)  $N = 275$ , (b)  $N = 250$ , (c)  $N = 200$ , and (d)  $N = 150$ .

to noise. We simulate one measurement matrix that applies to all three translations of the physical phantom. For each translation we simulate distinct bucket data and obtain a reconstruction. We patch the reconstructions together to form an overall reconstruction (see Sec. III B for more experimental details).

In Fig. 1 we show the measurement matrix for the BNL experiment. The average number of counts per element of the measurement matrix is  $2.56 \times 10^5$ . The average number of counts per component of the bucket data vectors is  $3.64 \times 10^6$ .

In our primary simulation study, the theoretical (true) measurement matrix  $\tilde{A}$  is equated to a scaled version of the observed measurement matrix shown in Fig. 1 where the scaling factor is 10. (When a matrix is multiplied by a scalar, each element of the matrix is multiplied by the scalar.) The digital phantom  $\tilde{v}$  is scaled so that the sum of the total expected counts in the three simulated bucket data vectors agrees with 10 times the sum of the counts in the three experimental bucket data vectors. Since the digital phantom [see Fig. 11(a)] is a rendition of the optical image of the physical phantom [see Fig. 11(b)], it has complexity similar to the physical phantom. We simulate  $A$  by adding Poisson noise to each

element of the theoretical measurement matrix  $\tilde{A}$ . For each translation we simulate bucket data by adding Poisson noise to the theoretical bucket signal  $\tilde{b}$  [see Eq. (1)]. We simulate  $A$  (with size  $442 \times 276$ ) and  $b$  with dimension 442, and then select subsets of  $A$  and  $b$ —the first  $N$  rows of  $A$  and the first  $N$  components of  $b$ .

In Fig. 2 we show reconstructions of noise-free data for  $P = 276$  where  $N$  varies from 100 to 275, and scatterplots of reconstructions and the digital phantom. We determine these reconstructions with our data augmentation method with the  $QR$  and TSVD methods. Since the data are noise-free, we set the relative threshold for the truncated SVD,  $\kappa_{\text{SVD}}$ , to the very low value of  $1.49 \times 10^{-8}$  based on machine precision considerations. Here we determine the TSVD with the function `ginv` in the R package **MASS** [31].

In our primary simulation study, we simulate 100 realizations of  $A$  and  $b$  for each of many values of  $N$ . For each realization of  $A$  and  $b$ , we determined a reconstruction for each of many values of  $\kappa_{\text{SVD}}$  on a grid. For each value of  $N$  and  $\kappa_{\text{SVD}}$ , we estimate the RMSE of the reconstruction. For each  $N$ ,  $\kappa_{\text{SVD}} = 10^{-4}$  yields the lowest RMSE. As a caveat, for  $N = 50, 75, 100$  values of  $\kappa_{\text{SVD}}$ , less than 0.0001 also yield

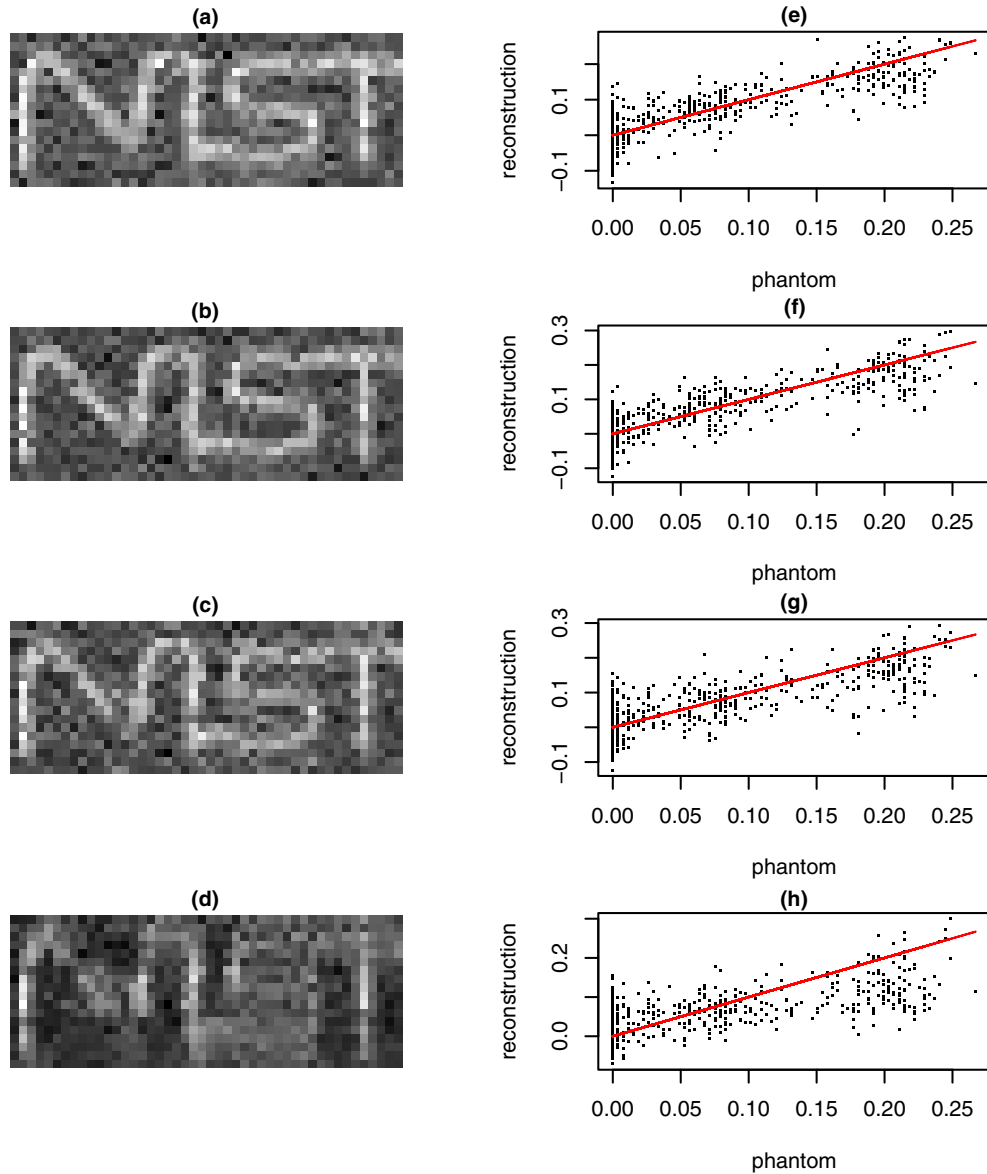


FIG. 5. We equate the theoretical measurement matrix to 10 times the experimental measurement matrix shown in Fig. 1. The number of pixels is  $P = 276$ . (a)–(d) Reconstructions of simulated noisy data for  $N = 275, 250, 200$ , and  $100$ . (e)–(h) Associated scatterplots of reconstruction and the digital phantom. Points that fall on the red line correspond to cases where the reconstruction and true value agree exactly.

the minimum value. If multiple values of  $\kappa_{\text{SVD}}$  yield the minimum RMSE, we report the largest of these values. In Fig. 3 we show reconstructions of noisy simulated data for the  $N = 275$  case for various values of  $\kappa_{\text{SVD}}$ . In Fig. 4 we show how Monte Carlo estimates of RMSE vary with  $\kappa_{\text{SVD}}$  for various values of  $N$ . In Fig. 5 we show reconstructions of simulated noisy data and associated scatterplots. In Fig. 6 we show denoised versions of the Fig. 5 reconstructions and associated scatterplots. In Fig. 7 we compare denoised reconstructions determined with our method and the method from Ref. [14].

For all cases considered, the RMSE of reconstructions obtained with our method are lower than the RMSE of reconstructions obtained with the method from [14] (see Table I). For our method RMSE decreases as  $N$  increases (see Table I). For the method from [14], RMSE decreases as  $N$  increases

from 50 to 150 but then increases as  $N$  increases from 150 to 275. The authors of [14] observed a similar instability as  $N$  increased and attributed the phenomenon to numerical instability effects. For both methods, denoised reconstructions have lower RMSE than reconstructions that are not denoised with AWS (see Table I).

## B. Experimental results

We acquired experimental data at the National Synchrotron Light Source II at Brookhaven National Laboratory (BNL) at the NIST Beamline for Materials Measurement (BMM) (see Fig. 8). The energy of the incident x-ray beam was 12 keV (see Fig. 9). The cross-sectional area of the incident x-ray beam, set by four-blade tungsten slits, was  $8 \text{ mm} \times 1 \text{ mm}$ . We acquired measurement matrix data with a Dectris Pilatus 2D

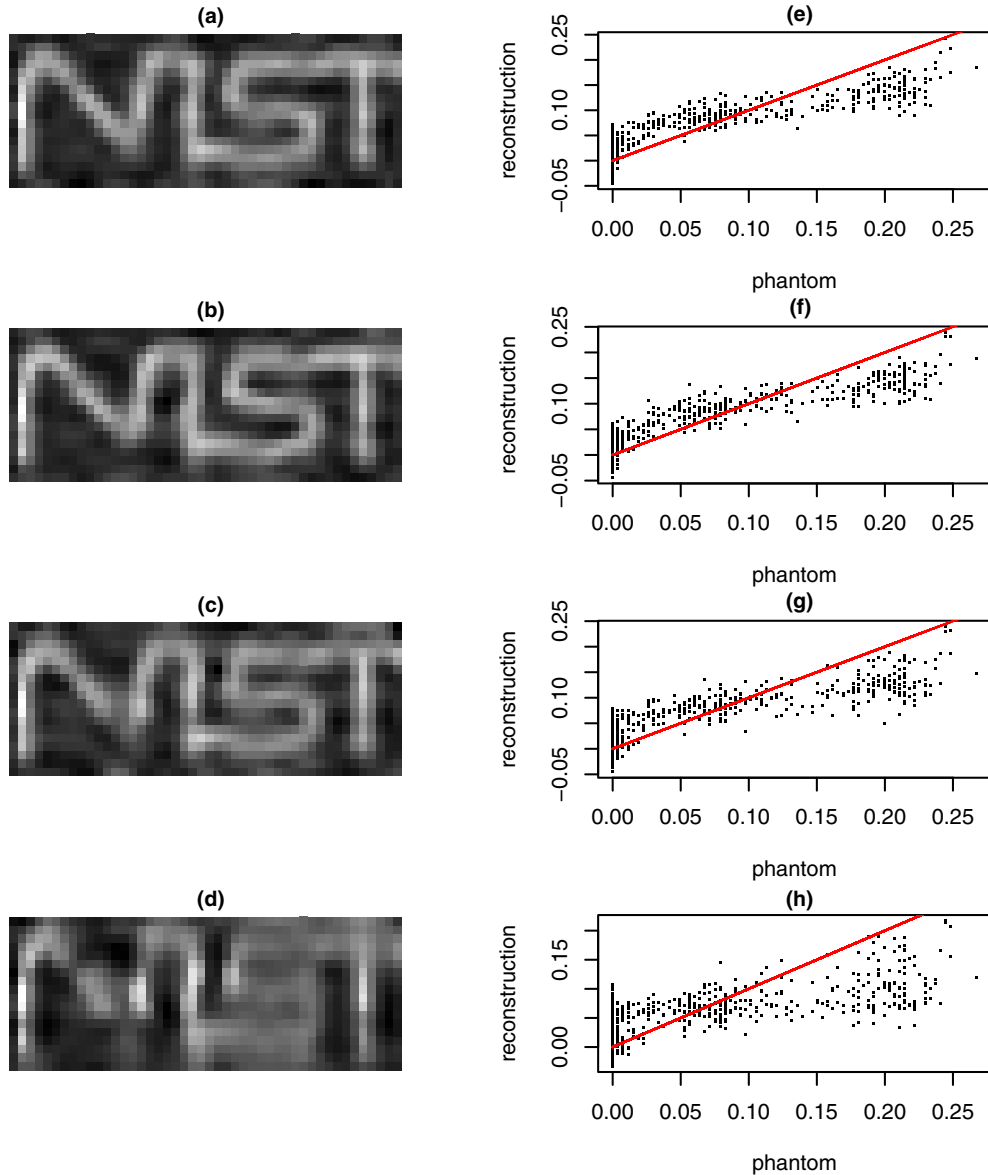


FIG. 6. Here we show denoised versions of the Fig. 5 reconstructions. (a)–(d) Denoised reconstructions for  $N = 275, 250, 200,$  and  $100$ . (e)–(h) Associated scatterplots of denoised reconstruction and digital phantom. Points that fall on the red line correspond to cases where the reconstruction and true value agree exactly.

silicon hybrid photon counting imaging detector. In this detector the pixel width is approximately  $0.172$  mm. We monitored beam intensity with ionization chambers (standard beamline equipment) during both the setup stage and the primary stage of the experiment.

The barcode mask was fabricated by patterning and etching arrays of trenches in a Si wafer, metalizing the entire surface with a sputtered Au seed layer and then applying an additive-based electrochemical deposition process to selectively fill the trenches with gold from the bottom upward [32,33]. Distinct orientations of the mask were produced by translating the mask (ideally) in the  $x$  direction (see Fig. 10). For  $i = 1, 2, \dots, 442$ , the  $i$ th translation was  $(i-1) 50 \mu\text{m}$ . Since there are 276 pixels in the imaging detector, the size of the measurement matrix is  $442 \times 276$  (see Fig. 1).

The physical phantom consists of a copper wire [see Fig. 11(b)] that is shaped to spell out “NIST.” When placed behind the mask and irradiated with x rays, it emitted an x-ray fluorescence spectrum. At each mask orientation, for each translation of the physical phantom, the associated bucket signal is the number of counts in the Cu  $k$ -edge fluorescence peaks. This spectrum was acquired with a four-element Si drift detector with Quantum Electronic XSpres 3X counting electronics.

As mentioned earlier, the narrow beam width necessitated three measurements to cover the entire height of the phantom. Bucket data was acquired for each of three translations of the physical phantom. The translations (in the  $y$  direction) were  $0 \delta, 6 \delta,$  and  $12 \delta$ , where  $\delta \approx 0.172$  mm is the width of each pixel in the imaging detector. The rectangular areas associated with



TABLE I. Estimated expected value of RMSE of reconstructions for primary simulation study. Theoretical measurement matrix equated to 10 times the experimental measurement matrix shown in Fig. 1. (a) Estimated RMSE of data augmentation reconstruction. (b) Estimated RMSE of reconstruction determined with method from [14]. (c) Ratio of (b) and (a). (d) Estimated RMSE of denoised data augmentation reconstruction. (e) Estimated RMSE of denoised reconstruction determined with method from [14]. (f) Ratio of (e) and (d).

N	(a)	(b)	(c)	(d)	(e)	(f)
50	0.0608	0.065	1.07	0.0616	0.0643	1.04
75	0.0570	0.0604	1.06	0.0555	0.0569	1.02
100	0.0547	0.0580	1.06	0.0524	0.0531	1.01
150	0.0499(1)	0.0522(1)	1.04	0.0427	0.0427	1.00
200	0.0470(1)	0.0644(3)	1.37(1)	0.0384	0.0400(1)	1.04
225	0.0452(1)	0.0811(6)	1.79(1)	0.0367	0.0413(1)	1.12
250	0.0435(1)	0.1310(14)	3.01(3)	0.0352(1)	0.0505(2)	1.44(1)
260	0.0429(1)	0.1880(26)	4.39(6)	0.0346	0.0642(5)	1.85(2)
265	0.0428(1)	0.2450(42)	5.71(10)	0.0344(1)	0.0789(9)	2.29(3)
270	0.0425(1)	0.3780(130)	8.88(31)	0.0341(1)	0.1090(17)	3.20(5)
275	0.0423(1)	0.8020(441)	19.00(104)	0.0340(1)	0.3610(348)	10.60(102)

the translations did not overlap. For each translation we obtain a reconstruction of size  $6 \times 46$ . We patch these reconstructions together to form an overall reconstruction of size  $18 \times 46$ .

In our experimental study, based on the measurement matrix shown in Fig. 1, we determine reconstructions of experimental data without the  $QR$  step and with the  $QR$  and TSVD steps [see Figs. 11(d) and 11(h)]. We show denoised versions of these reconstructions in Figs. 11(f) and 11(j). Based on visual inspection, the denoised reconstruction of experimental data determined with the  $QR$  and TSVD steps [see Fig. 11(j)] appears to reveal the “N” and “T” features more clearly than the denoised reconstruction determined without

the  $QR$  step [see Fig. 11(f)]. In both of these reconstructions, the “N,” “I,” and “T” features are visible; however, the “S” feature is not visible in either reconstruction. Overall, it appears that the Fig. 11(j) reconstruction is better than the Fig. 11(f) reconstruction.

As a diagnostic check, we simulate data based on the Fig. 1 measurement matrix. In this simulation the expected number of counts in the observed measurement matrix and the sum of the expected counts in the three bucket data vectors agree with the BNL experiment. The denoised reconstruction of the simulated data determined with the  $QR$  and TSVD steps [see Fig. 11(i)] is vastly superior to the denoised reconstruction of simulated data determined without the  $QR$  and without the TSVD step [see Fig. 11(e)]. However, for the experimental data the denoised reconstruction with the  $QR$  and with the TSVD step is better but not vastly superior to the denoised reconstruction without the  $QR$  and without the TSVD step. Further, the denoised reconstruction of the simulated data determined with the  $QR$  and TSVD steps [see Fig. 11(i)] is vastly superior to the denoised reconstruction of experimental data determined with the  $QR$  and TSVD steps [see Fig. 11(j)]. (The above remarks about denoised reconstructions apply to comparisons of reconstructions as well.) Plausible systematic errors that might explain these results are relative mask

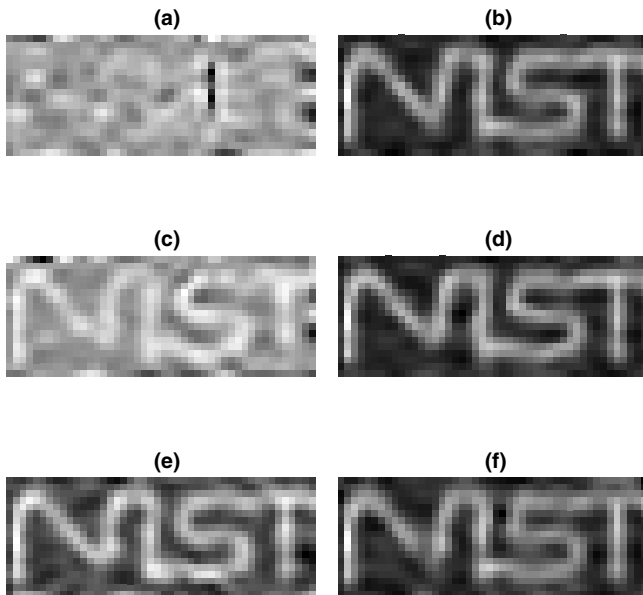


FIG. 7. We equate the theoretical measurement matrix to 10 times the experimental measurement matrix shown in Fig. 1. The number of pixels is  $P = 276$ . We show denoised reconstructions of simulated noisy data. (a), (c), and (e) Reconstructions determined with the method from [14] for  $N = 275$ , 250, and 200. (b), (d), and (f) Reconstructions determined with our method for  $N = 275$ , 250, and 200.

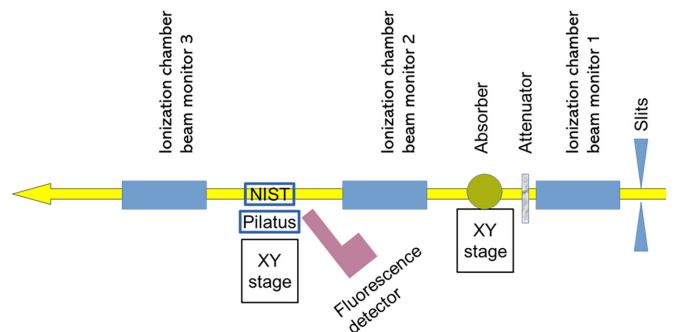


FIG. 8. Experimental setup at the NIST Beamline for Materials Measurement at the National Synchrotron Light Source II at Brookhaven National Laboratory.

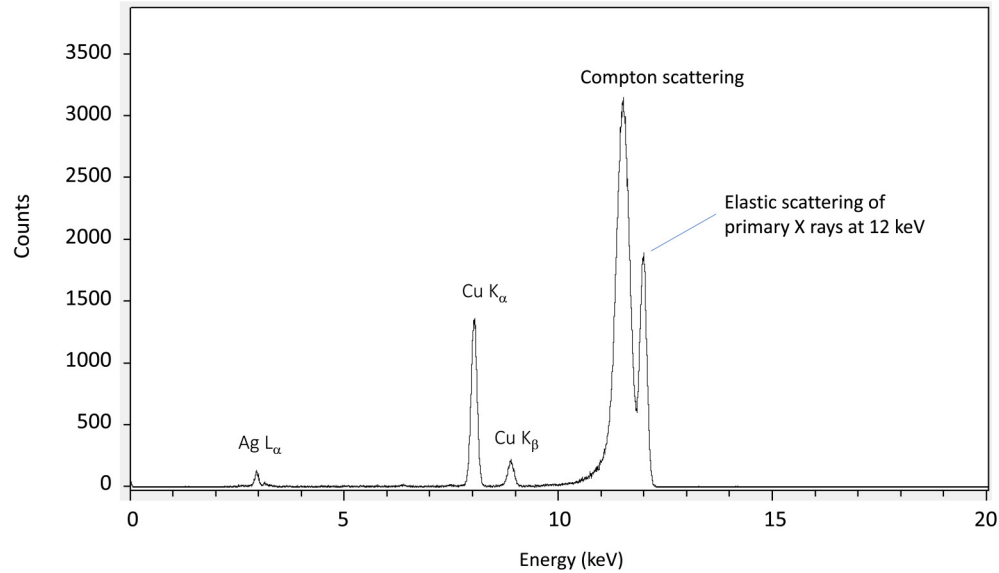


FIG. 9. An x-ray fluorescence spectrum excited by a monochromatic x-ray beam at 12 keV incident on the physical phantom made with copper wire [see photograph in Fig. 11(b)]. The bucket signal is obtained by summing the counts under the Cu  $K_{\alpha}$  and Cu  $K_{\beta}$  peaks. X rays that undergo elastic scattering or Compton scattering do not contribute counts to the bucket data.

orientation errors in the experiment that acquires the measurement matrix, and the experiment that acquires the bucket data.

In an attempt to suppress relative mask orientation errors in the two experiments, we aggregate the measurement matrix and bucket data. In this scheme the measurement matrix elements in each column are grouped into blocks of size  $m$ . For instance, if  $m=3$ , the first three elements go into the

first block. The next three go into the second block, and so on. Elements in each block are summed. A similar procedure applies to the bucket data. For the  $m=3$  choice, the number of rows in  $A$  is reduced from 442 to 147. Similarly, the number of components in  $b$  is reduced from 442 to 147. In three aggregation schemes, the number of rows in  $A$  and the dimension of the bucket data are reduced from 442 to

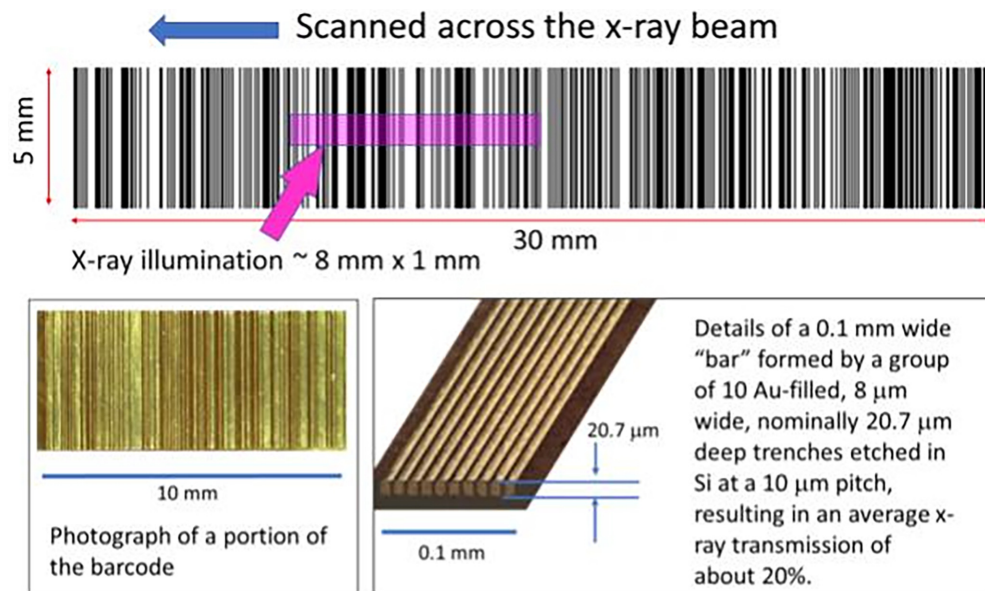


FIG. 10. The computer-designed barcode mask was fabricated by bottom-up gold filling of nominally 20.7- $\mu\text{m}$ -deep trenches patterned and etched into the surface of a silicon wafer. The “gold bars in the barcode pattern are actually arrays of 8- $\mu\text{m}$ -wide Au-filled trenches and 2- $\mu\text{m}$ -wide Si spacers that have been repeated as needed for the bar width. Illumination of the system was defined by stepping the barcode mask through a sequence of 50- $\mu\text{m}$  displacements parallel to the barcode, generating a total of 442 spatial patterns that were captured by a CCD camera. The same sequence of illumination patterns was repeated with the specimen in place for x-ray fluorescence data acquisition. The patterns and the corresponding x-ray fluorescence signals were processed offline for ghost imaging reconstruction.

Method \ Phantom		Simulation	Experiment
		(a)	(b)
Reconstruction ( $N = 442, P = 276$ ) w/o QR	w/o AWS	(c)	(d)
	with AWS	(e)	(f)
Reconstruction ( $N = 442, P = 276$ ) with QR, TSVD	w/o AWS	(g)	(h)
	with AWS	(i)	(j)
Reconstruction ( $N = 147, P = 276$ ) with QR, TSVD	with AWS		(k)

FIG. 11. In the “Simulation” column, we show the digital phantom and reconstructions and denoised reconstructions of simulated data with signal-to-noise similar to experimental data. In the “Experiment” column, we show the physical phantom and reconstructions and denoised reconstructions of experimental data. For all cases the number of pixels is  $P = 276$ . Except for (k), the number of mask orientations is  $N = 442$ . In an effort to suppress systematic errors, we aggregate the experimental data so that  $N$  is reduced from 442 to 147. To enable analysis with the  $QR$  and TSVD steps, we augment the aggregated data so that  $N = 294$ . In (k) we show the denoised reconstruction of the augmented data.

147, 110, and 55, respectively. After data augmentation, the associated resulting denoised reconstructions for the three aggregation schemes are not dramatically improved relative to the denoised reconstruction computed from the full data with the  $QR$  and TSVD steps. Based on visual inspection, the aggregation scheme corresponding to 147 rows in  $A$  [see Fig. 11(k)] appears to produce a slightly better result than the other aggregation schemes.

As discussed in Sec. II B, when reconstructing experimental data with a  $QR$  step, we determine a reconstruction for each of 101 permutations of the columns of the measurement matrix. For each pixel we report the median value of the associated 101 reconstructions. To understand how results vary with the number of permutations  $N_p$ , for the  $N = 442$  case we determine a reference reconstruction at  $N_p = 1001$ . For this case reconstructed values fall in the interval  $(-0.049, 0.558)$ , and denoised reconstructed values fall in the interval  $(-0.041, 0.313)$ . We determine a reconstruction from the observed measurement matrix ( $N_p = 0$ ) and reconstructions at  $N_p = 5, 11, 25, 51, 101$ . At each pixel we compute the

difference  $\Delta$  between each reconstruction and the reference reconstruction and the difference  $\Delta_{dn}$  between each denoised reconstruction and the denoised reference reconstruction. In Table II we show the minimum and maximum value of  $\Delta$  and  $\Delta_{dn}$  for each value of  $N_p$ .

Based on Table II, it appears that the choice of  $N_p = 11$  (or higher) yields sufficiently stable results. For simulated data

TABLE II. Stability of reconstructions and denoised reconstructions of experimental data determined with  $QR$  and TSVD steps as a function of the number of permutations  $N_p$ .

$N_p$	$\min(\Delta)$	$\max(\Delta)$	$\min(\Delta_{dn})$	$\max(\Delta_{dn})$
0	$-1.04 \times 10^{-1}$	$4.98 \times 10^{-2}$	$-9.02 \times 10^{-2}$	$2.99 \times 10^{-2}$
5	$-5.10 \times 10^{-4}$	$4.63 \times 10^{-4}$	$-2.37 \times 10^{-4}$	$2.13 \times 10^{-4}$
11	$-1.13 \times 10^{-4}$	$1.63 \times 10^{-4}$	$-5.78 \times 10^{-5}$	$9.40 \times 10^{-5}$
25	$-1.28 \times 10^{-4}$	$1.35 \times 10^{-4}$	$-7.45 \times 10^{-5}$	$2.31 \times 10^{-4}$
51	$-7.99 \times 10^{-5}$	$8.91 \times 10^{-5}$	$-8.38 \times 10^{-5}$	$2.56 \times 10^{-5}$
101	$-5.06 \times 10^{-5}$	$3.45 \times 10^{-5}$	$-2.25 \times 10^{-5}$	$1.36 \times 10^{-5}$

we expect that reconstructions (determined with a  $QR$  step) are also sufficiently stable for  $N_p = 11$  (or higher).

#### IV. DISCUSSION

Our research on data augmentation was motivated by the goal of understanding x-ray fluorescence emission rate measurements determined with ghost imaging. In future experiments we plan to investigate possible mask orientation errors that may have affected our measurements.

For reconstructions obtained from simulated data without the  $QR$  step and without the column permutation method, it is straightforward to show that the reconstruction of the original data and the reconstructions of its augmented versions agree exactly (if computed with an infinite precision computer). This observation is consistent with the claim that data augmentation is a reasonable procedure.

For the cases studied, for reconstructions determined with the  $QR$  step, the predicted number of total counts in the bucket data agrees with the observed number of total counts in the bucket data to six significant digits or more. This observation is consistent with the claim that our Eq. (9) approach is valid.

For simulated data shown in Fig. 2(e), reconstruction and phantom values are nearly the same. This observation is consistent with the claim that our Eq. (9) approach is valid. Results shown in Figs. 2(f), 5(e), and 5(f) also support the above claim.

For the case where  $N = 442$  and  $P = 276$ , we reconstructed high signal-to-noise simulated data (with  $\kappa_{\text{SVD}} = 10^{-6}$ ) as well as its augmented versions where  $N = 884$ , 1326, and 1768 with  $QR$  but without permutation of the columns of the measurement matrix. The RMSE values for reconstructions for  $N = 442$ , 884, 1326, and 1768 are 0.0278, 0.0281, 0.0280, and 0.0279. The RMS deviation between the reconstruction of the  $N = 442$  data, and reconstructions at  $N = 884$ , 1326, and 1768 are 0.0010, 0.0008, and 0.0011. Scatterplots show that the reconstructions of the augmented data and the  $N = 442$  data are almost the same. Even though data augmentation is not expected to improve reconstructions for the  $N > P$  case considered in this simulation study, data augmentation did not significantly degrade the reconstruction. This diagnostic study suggests that data augmentation is reasonable.

In simulation studies, for the  $N < P$  case our method yields reconstructions with lower RMSE compared to the method from [14]. This is plausible because the Gram-Schmidt orthogonalization scheme implemented in [14] may be unstable compared to the  $QR$  scheme that we implement in our method. See Ref. [7] for discussion of this point. Second, the TSVD step in our method improves results (especially for large  $N$ ) (see Fig. 4). Another possibility is that our method performs better because we account for the  $PSF$  function whereas the method in [14] does not.

In our primary simulation study, the theoretical measurement matrix was equated to 10 times the experimental measurement matrix shown in Fig. 1. For each  $N$ , RMSE took its minimum value when  $\kappa_{\text{SVD}} = 10^{-4}$ . In a secondary simulation study, the theoretical measurement matrix was equated to the experimental measurement matrix shown in Fig. 1. For each  $N$ , the relative RMSE for the method from [14]

increased relative to our method. For  $N \leq 100$ , RMSE takes its minimum value at  $\kappa_{\text{SVD}} = 10^{-3}$ . For each  $N$  above 100, RMSE takes its minimum value at  $\kappa_{\text{SVD}} = 5 \times 10^{-4}$ . Since the data is noisier in the secondary study, it makes sense that a larger  $\kappa_{\text{SVD}}$  is required to minimize RMSE.

We remark that compressive sensing has been broadly applied to reflection ghost imaging [10], transmission ghost imaging [34,35], and recently to emission ghost imaging [11]. Compressive sensing methods are appropriate for cases where signals of interest are sparse. In ghost imaging applications, signals of interest are typically sparse. For the case where signals of interest are not sparse, we expect the performance of compressive sensing methods to deteriorate. In contrast, we expect our method to apply to both sparse and nonsparse signals of interest. We expect compressive sensing to apply to the  $N < P$  case. For the data analyzed here, comparison of our method to the compressive sensing method is a worthy topic for future research but beyond the scope of this study. Other methods relevant to the  $N < P$  case include pseudoinverse methods [9,36], singular value decomposition methods [37], and deep learning [27,38–40].

For analysis of experimental data, we selected the threshold for the truncated SVD method by visual inspection of the reconstructions determined with different thresholds for the truncated SVD method. Future research will focus on data-driven threshold selection methods such as cross-validation or related methods (see, for example [41]).

As stated earlier, the AWS denoising method is designed to smooth out noise and preserve edges in images. In our simulation study, the denoised versions of the Fig. 5 reconstructions (shown in Fig. 6) have well-preserved edges and noise is significantly suppressed. A similar comment applies to the denoised version of the Fig. 11(g) reconstruction that is shown in Fig. 11(i).

In this work we report RMSE statistics. As discussed in [42], there are other candidate metrics as well. For example, how well the mean value of  $\tilde{v}$  is determined in a region of interest is a possible alternative metric. We note that other metrics were studied in [14]. How well our method performs for higher-dimensional cases is a topic for further study.

In our simulation studies, for the cases studied we demonstrated that denoising ghost imaging reconstructions with AWS reduces RMSE. However, in some analyses it may be best to extract quantitative information from reconstructions rather than denoised reconstructions. For instance, it may be best to determine the mean emission yield in a region of interest as the sample mean of reconstructed emission yields.

We expect our methods for ghost imaging to be directly applicable to other emission signals, including neutron capture prompt  $\gamma$  rays. Our long-term goal is to develop methods for elemental mapping based on ghost imaging of neutron capture prompt  $\gamma$  rays.

#### ACKNOWLEDGMENTS

Research performed, in part, at the NIST Center for Nanoscale Science and Technology. We thank C. Daugherty, M. Frey, and J. Prothero of NIST for helpful comments. Certain commercial equipment, instruments, or materials are identified in this paper to foster understanding. Such

identification does not imply recommendation or endorsement by the National Institute of Standards and Technology, nor

does it imply that the materials or equipment identified are necessarily the best available for the purpose.

- 
- [1] T. B. Pittman, Y. H. Shih, D. V. Strekalov, and A. V. Sergienko, *Phys. Rev. A* **52**, R3429(R) (1995).
- [2] M. J. Padgett and R. W. Boyd, *Philos. Trans. R. Soc. A* **375**, 20160233 (2017).
- [3] Y. Bromberg, O. Katz, and Y. Silberberg, *Phys. Rev. A* **79**, 053840 (2009).
- [4] H. Yu, R. Lu, S. Han, H. Xie, G. Du, T. Xiao, and D. Zhu, *Phys. Rev. Lett.* **117**, 113901 (2016).
- [5] D. Pelliccia, A. Rack, M. Scheel, V. Cantelli, and D. M. Paganin, *Phys. Rev. Lett.* **117**, 113902 (2016).
- [6] D. Pelliccia, M. P. Olbinado, A. Rack, A. M. Kingston, G. R. Myers, and D. M. Paganin, *IUCrJ* **5**, 428 (2018).
- [7] D. Ceddia and D. M. Paganin, *Phys. Rev. A* **97**, 062119 (2018).
- [8] S. Li, F. Cropp, K. Kabra, T. J. Lane, G. Wetzstein, P. Musumeci, and D. Ratner, *Phys. Rev. Lett.* **121**, 114801 (2018).
- [9] A. M. Kingston, G. R. Myers, D. Pelliccia, F. Salvemini, J. J. Bevitt, U. Garbe, and D. M. Paganin, *Phys. Rev. A* **101**, 053844 (2020).
- [10] C. Zhao, W. Gong, M. Chen, E. Li, H. Wang, W. Xu, and S. Han, *Appl. Phys. Lett.* **101**, 141123 (2012).
- [11] Y. Klein, O. Sefi, H. Schwartz, and S. Shwartz, *Optica* **9**, 63 (2022).
- [12] M. Manni, A. Ben-Yehuda, Y. Klein, B. Lukic, A. Kingston, A. Rack, S. Shwartz, and N. Viganò, *Opt. Lett.* **48**, 6271 (2023).
- [13] A. M. Kingston, W. K. Fullagar, G. R. Myers, D. Adams, D. Pelliccia, and D. M. Paganin, *Phys. Rev. A* **103**, 033503 (2021).
- [14] B. Luo, P. Yin, L. Yin, G. Wu, and H. Guo, *Opt. Express* **26**, 23093 (2018).
- [15] C. Shorten and T. M. Khoshgoftaar, *J. Big Data* **6**, 60 (2019).
- [16] T. Hu, T. Tang, and M. Chen, *IEEE Access* **7**, 125133 (2019).
- [17] E. H. Moore, *Bull. Am. Math. Soc.* **26**, 394 (1920).
- [18] R. Penrose, in *Mathematical Proceedings of the Cambridge Philosophical Society* (Cambridge University Press, Cambridge, England, 1955), Vol. 51, pp. 406–413.
- [19] G. Strang, *Linear Algebra and Its Applications* (Academic Press, New York, 1980).
- [20] P. C. Hansen, T. Sekii, and H. Shibahashi, *SIAM J. Sci. Stat. Comput.* **13**, 1142 (1992).
- [21] N. G. Gençer and S. J. Williamson, *IEEE Trans. Biomed. Eng.* **45**, 827 (1998).
- [22] L.-Y. Chen, C. Wang, X.-Y. Xiao, C. Ren, D.-J. Zhang, Z. Li, and D.-Z. Cao, *Opt. Express* **30**, 6248 (2022).
- [23] J. Polzehl and V. Spokoiny, *Ann. Stat.* **31**, 30 (2003).
- [24] J. Polzehl and V. Spokoiny, *Probab. Theory Relat. Fields* **135**, 335 (2006).
- [25] J. Polzehl, K. Papafitsoros, and K. Tabelow, *J. Stat. Software* **95**, 1 (2020).
- [26] J. Kim, J. Hwang, J. Kim, K. Ko, E. Ko, and G. Cho, *Opt. Express* **29**, 39323 (2021).
- [27] H. Wu, R. Wang, G. Zhao, H. Xiao, J. Liang, D. Wang, X. Tian, L. Cheng, and X. Zhang, *Opt. Lasers Eng.* **134**, 106183 (2020).
- [28] X.-R. Yao, W.-K. Yu, X.-F. Liu, L.-Z. Li, M.-F. Li, L.-A. Wu, and G.-J. Zhai, *Opt. Express* **22**, 24268 (2014).
- [29] J. Shao, *Mathematical Statistics* (Springer Science & Business Media, New York, 2003).
- [30] R Core Team, *R: A Language and Environment for Statistical Computing* (R Foundation for Statistical Computing, Vienna, Austria, 2023).
- [31] W. N. Venables and B. D. Ripley, *Modern Applied Statistics with S-PLUS* (Springer Science & Business Media, New York, 2013).
- [32] D. Josell, W. A. Osborn, M. E. Williams, and H. Miao, *J. Electrochem. Soc.* **169**, 032509 (2022).
- [33] D. Josell, Z. Shi, K. Jefimovs, V. A. Guzenko, C. Beauchamp, L. Peer, M. Polikarpov, and T. P. Moffat, *J. Electrochem. Soc.* **168**, 082508 (2021).
- [34] O. Katz, Y. Bromberg, and Y. Silberberg, *Appl. Phys. Lett.* **95**, 131110 (2009).
- [35] V. Katkovnik and J. Astola, *J. Opt. Soc. Am. A* **29**, 1556 (2012).
- [36] C. Zhang, S. Guo, J. Cao, J. Guan, and F. Gao, *Opt. Express* **22**, 30063 (2014).
- [37] X. Zhang, X. Meng, X. Yang, Y. Wang, Y. Yin, X. Li, X. Peng, W. He, G. Dong, and H. Chen, *Opt. Express* **26**, 12948 (2018).
- [38] Y. He, G. Wang, G. Dong, S. Zhu, H. Chen, A. Zhang, and Z. Xu, *Sci. Rep.* **8**, 6469 (2018).
- [39] L. Zhang, Z. Bian, H. Ye, D. Zhang, and K. Wang, *Opt. Commun.* **504**, 127479 (2022).
- [40] S. Rizvi, J. Cao, K. Zhang, and Q. Hao, *Sci. Rep.* **10**, 11400 (2020).
- [41] A. B. Owen and P. O. Perry, *Ann. Appl. Stat.* **3**, 564 (2009).
- [42] H. H. Barrett, J. Denny, R. F. Wagner, and K. J. Myers, *J. Opt. Soc. Am. A* **12**, 834 (1995).